Evaluation of the performance of a lead-free piezoelectric material for energy harvesting

2015 Smart Mater. Struct. 24 115011

(http://iopscience.iop.org/0964-1726/24/11/115011)

IOP Publishing Smart Materials and Structures
Smart Mater. Struct. 24 (2015) 115011 (8pp) doi:10.1088/0964-1726/24/11/115011

Evaluation of the performance of a lead-free piezoelectric material for energy harvesting

S P Machado[1], M Febbo[2], F Rubio-Marcos[3], L A Ramajo[4] and M S Castro[4]

[1] Grupo de Investigación en multifísica aplicada, Universidad Tecnológica Nacional FRBB, 11 de Abril 461, 8000 Bahía Blanca, Argentina
[2] Instituto de Física del Sur (IFISUR), Consejo Nacional de Investigaciones Científicas y Técnicas (CONICET) and Departamento de Física. Universidad Nacional del Sur (UNS). Av Alem 1253, 8000 Bahía Blanca, Argentina
[3] Electroceramic Department, Instituto de Cerámica y Vidrio, CSIC, Kelsen 5, 28049, Madrid, Spain
[4] División Cerámicos, INTEMA, CONICET-UNMdP, Avda. Juan B. Justo 4302, B7068FDQ Mar del Plata, Buenos Aires, Argentina

E-mail: mfebbo@uns.edu.ar

Received 20 March 2015, revised 10 August 2015
Accepted for publication 30 August 2015
Published 7 October 2015

Abstract

Vibration-based energy harvesting has been explored as an auxiliary power source, which can provide small amounts of energy to power remote sensors installed in inaccessible locations. This paper presents an experimental and analytical study of an energy harvesting device using a lead-free piezoelectric material based on MoO_3-doped $(K_{0.44}Na_{0.52}Li_{0.04})(Nb_{0.86}Ta_{0.10}Sb_{0.04})O_3$ KNL-(NTS)Mo. The harvesting model corresponds to a cantilever beam with a KNL-(NTS)Mo piezoelectric disc attached to it. We analyze the effect of electromechanical coupling and load resistance on the generated electrical power. Electromechanical frequency response functions that relate the voltage output to the translational base acceleration are shown for experimental and analytical results.

Keywords: lead-free piezoelectric, vibration, energy harvesting

(Some figures may appear in colour only in the online journal)

1. Introduction

Energy harvesting is one of the most promising techniques as an alternative for the implementation of renewable energy as a long-term sustainable solution to the energy problem. Energy harvesting sources include solar power [1], thermal gradients [2], ocean waves [3], human body movements [4] and vibration [5, 6]. In recent years many researchers have concentrated their attention on the use of mechanical vibration as potential power for energy harvesting. Harvesters can be miniaturized and do not require an external voltage source [7–9]. For this purpose, materials with high electromechanical coupling are required.

In the vast majority of piezoelectric energy harvesting applications, the most common type of piezoelectric material used is lead zirconate titanate (PZT) [10–13]. However, a number of different piezoelectric materials have been developed over the years. The type of piezoelectric material selected for a power harvesting application can have a major influence on the functionality and performance of the harvester. Although PZT is widely used as a power harvesting material, the toxicity of lead is a serious health and environmental threat and thus lead-free piezoelectric ceramics have attracted significant attention. Numerous studies on lead-free piezoelectric ceramics such as (K,Na)NbO_3, $BaTiO_3$-based, Bi-layered, bismuth sodium titanate and tungsten bronze-type materials have been published recently [14–16]. Niobates (K,Na)NbO_3 (KNN)-based ceramics have shown good piezoelectric and electrical properties, high Curie temperature and are environmentally benign. Saito *et al* [17] reported exceptionally high piezoelectric properties for the (K,Na)NbO_3 LiTaO_3 LiSbO_3 system. Their study was based on chemical modifications, in the vicinity of the morphotropic phase boundary (MPB) of KNN, by complex simultaneous substitutions in the A (Li) and B (Ta and Sb) site of the perovskite lattice. In addition, KNN-based ceramics with

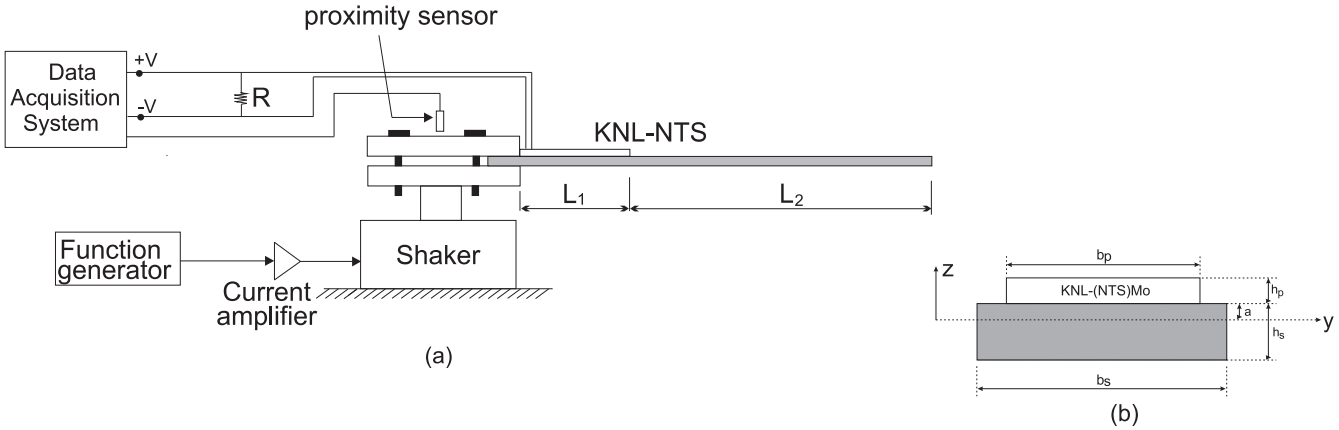

Figure 1. (a) Schematic diagram of the experimental setup. (b) Cross-sectional view of the electromechanical system.

4 mol % of lithium, 10 mol % of tantalum and 4 mol % of antimony present interesting piezoelectric properties [18]. In the present paper, we used MoO_3-doped lead-free $(K_{0.44}Na_{0.52}Li_{0.04})(Nb_{0.86-x}Ta_{0.1-x}Sb_{0.04-x})Mo_{5/6x}O_3$, hereafter abbreviated as KNL-(NTS)Mo, as a novel material to harvest vibration energy.

In the early mathematical modelling of piezoelectric energy harvesters, researchers employed a lumped-parameter model to predict the dynamics of the electromechanical system comprising a flexible metallic (steel) beam and a piezoceramic element attached to it. This was the main procedure followed by Roundy and Wright [19] and duTouit *et al* [20]. Although this model offers insight into the problem, it lacks some important aspects of the coupled electromechanical problem such as the dynamic mode shapes of the composite and accurate strain distributions that contribute to the correct estimation of the electrical response. Analytical solutions based on a distributed-parameter model were given by Erturk and Inman [21, 22] along with experimental validation of the proposed models. They used vibration mode shapes under the Bernoulli–Euler beam theory and constitutive piezoelectric relations to obtain the coupled electromechanical equations.

The aim of the present work is to study a novel piezoelectric material made of KNL-(NTS)Mo employed to harvest energy from a vibrating system. The piezoelectric disc is attached to a steel beam subjected to base vibration in order to generate electric power. The intention is to contrast the analytical model with experimental results. Additionally, optimization of the generated power is studied by analyzing the effect of the resistive load in the electric circuit of the electromechanical system.

2. Mathematical model

The system under study is presented in figure 1. It comprises KNL-(NTS)Mo lead-free piezoelectric material attached up to L_1 to a steel beam of total length L_2 that acts as its support.

The whole system is base-excited by deterministic function $g(t)$, which tries to mimic an environmental excitation from which energy can be extracted. In order to model the electromechanical system, we considered the system (beam and piezoelectric disc) as two separate Euler–Bernoulli beams satisfying continuity and compatibility conditions at their junction [23]. The final electromechanical expression that yields the voltage generation of mode j in terms of the system parameters can be found elsewhere [22]:

$$\overline{v} = \frac{\Gamma_j \theta_j \Omega R_l}{\sqrt{\left(\omega_j^2 - \Omega^2 - 2C_p R_l \xi_j \omega_j \Omega^2\right)^2 + \left(2\Omega\xi_j\omega_j + R_l\Omega\left(\theta_j^2 + C_p\omega_j^2 - C_p\Omega^2\right)\right)^2}}, \quad (1)$$

where $e_{zx} = d_{31}c_{11}^E$, d_{31} is the piezoelectric constant and c_{11}^E is the Young modulus of the piezoelectric element at constant electric field. The other parameters are: Ω excitation frequency, R_l resistive load, C_p internal capacitance of the piezoelectric disc, ω_j jth natural frequency of the system and ξ_j jth modal damping. The dynamical parameters that represent the electromechanical coupling are: the piezoelectric coupling of mode j,

$$\theta_j = \frac{e_{zx}}{2} b_p \frac{\left(a h_p + \frac{h_p^2}{2}\right)}{h_p} \phi'_j(L_1)$$

(see figure 1(b) for the definition of constants) and the modal coupling

$$\Gamma_j = \rho_1 A_1 \int_0^{L_1} \Phi_{j,1} \mathrm{d}x + \rho_2 A_2 \int_{L_1}^{L_1+L_2} \Phi_{j,2} \mathrm{d}x.$$

Due to the large thickness of the piezoelectric disc compared with that of the steel beam (two times larger than the beam), we decided to add its flexural rigidity in obtaining the total mode shape of the system ϕ_j. Finally, taking into account the above considerations ϕ_j can be written as

$$\phi_j(x) = \sum_{k=1}^{2} \Phi_{j,k}(x) H_k(x), \quad (2)$$

where k is the number of sections and $H_k(x)$ is the Heaviside function to denote the break at $x = L_1$. Considering the

piezoelectric laminate $\Phi_{j,1}$ results in

$$\Phi_{j,1}(x) = C_1 \sin(\beta_{j,1}x) + C_2 \cos(\beta_{j,1}x) + C_3 \sinh(\beta_{j,1}x) + C_4 \cosh(\beta_{j,1}x), \quad (3)$$

where C_i represent constants determined by the boundary conditions and $\beta_{j,1}$ are the eigenvalues given by $\beta_{j,1}^4 = \omega_j^2 \rho_1 A_1 / (E_1 I_1)$. The L_1 sectional properties are given by integrating $1/2 \int_S z^2 E_{(s/p)}\, dydz$ over the cross-sectional area S where E_s stands for the Young modulus of the substrate (steel beam) and $E_p = c_{11}^E$. This gives

$$E_1 I_1 = \frac{1}{12} b_s E_s h_s^3 + 2 b_p E_p \left(\frac{h_p^3}{3} + \frac{h_p^2 h_s}{2} + \frac{h_p h_s^2}{4} \right), \quad (4)$$

$$\rho_1 A_1 = 2 b_p h_p \rho_p + b_s h_s \rho_s. \quad (5)$$

For the L_2 section, the solution is

$$\Phi_{j,2}(x) = C_5 \sin(\beta_{j,2}x) + C_6 \cos(\beta_{j,2}x) + C_7 \sinh(\beta_{j,2}x) + C_8 \cosh(\beta_{j,2}x) \quad (6)$$

and C_{5-8} are determined by boundary conditions. In this case, the eigenvalues are $\beta_{j,2}^4 = \omega_j^2 \rho_2 A_2 / (E_2 I_2)$. Similarly, the L_2 sectional properties are given by

$$E_2 I_2 = \frac{1}{12} b_s E_s h_s^3, \quad (7)$$

$$\rho_2 A_2 = b_s h_s \rho_s. \quad (8)$$

To simplify the electromechanical model, we replace the disc for a rectangle of the same area with its length equal to the diameter of the disc. This approximation greatly simplifies the calculations and gives very good results, as is shown in the following sections.

3. Experimental details of the harvester fabrication

The sample composition used here (KNL-(NTS)Mo) was selected from previous studies on KNN-based lead-free piezoelectric ceramics [24].

3.1. Sample preparation

The compositional ceramic of KNL-(NTS)Mo was prepared by a conventional solid-state reaction from an adequate mixture of corresponding oxides and carbonates and calcinations at 700 °C for 2 h [18]. The ceramics were sintered for 2 h at 1125 °C. The amount of Li, Ta modifiers were, chosen to set the orthorhombic–tetragonal phase transition somewhere around room temperature, while Mo was added nominally as a B-site dopant in order to increase the grain size and to reduce conductivity.

3.2. Structural characterization

The crystalline structure was determined by x-ray diffraction analysis (XRD; X'Pert PRO Theta/2theta of Panalytical, Cu K_α radiation) on powder obtained by milling of the sintered ceramics. The lattice parameters were refined by a global simulation of the full diagram (pattern matching, *fullProf* program)

3.3. Microstructural characterization

Microstructure was evaluated on polished and thermally etched samples (1000 °C for 5 min) using a field emission scanning electron microscope (FE-SEM; Hitachi S-4700, Tokyo, Japan). The average grain size was determined from FE-SEM micrographs by an image processing and analysis program (Leica Qwin, Leica Microsystems Ltd, Cambridge, UK) considering more than 100 grains in each measurement.

3.4. Electrical characterization

Electrical characterization was carried out on ceramic discs with fire silver paste (700 °C) on both sides as electrodes. The ferroelectric nature of the ceramics was determined using a hysteresis meter (RT 6000 HVS, RADIANT Technologies) operating in virtual ground mode. The temperature dependence of the ceramics permittivity was measured using an impedance analyzer (HP4294A, Agilent) in the frequency range of 100 Hz−1 MHz and the temperature range 25–400 °C, using a 2 °C min^{-1} heating rate. The samples were polled in a silicon oil bath at 25 °C by applying a DC field of 4.0 kV mm^{-1} for 30 min. The piezoelectric constant d_{33} was measured using a piezo d_{33} meter (YE2730A d_{33} METER, APC International, Ltd, USA).

3.5. Overall characteristics

The x-ray diffraction pattern of the ceramic sample is shown in figure 2(a). The diffraction pattern corresponds to a perovskite phase without trace of secondary phases at room temperature, within the XRD resolution. The inset of figure 2(a) displays splitting of the (200) pseudo-cubic peak into (200) and (002), which suggests a non-cubic symmetry in this sample. The ceramic sample shows splitting that indicates the coexistence between a tetragonal symmetry T and an orthorhombic symmetry O, (see inset of figure 2(a)). Coexistence of different polymorphs (tetragonal and orthorhombic phases) was previously reported on KNL-NTS bulk ceramics [25, 26]. It is well known that the tetragonal symmetry of the perovskite phase can be deconvoluted into two peaks—$(002)_T$ and $(200)_T$—fit to a Lorentzian. However, in these patterns it is also seen that two more peaks appear at ~45.4 and ~45.6° (2Θ), which are associated with the orthorhombic symmetry. Nonetheless, refinement of the lattice parameters confirms that the tetragonal symmetry dominates in this ceramic sample. From figure 2(b), it can be observed that the ceramic sample has dense microstructure and a typical feature of quadrate-shaped grains, which is common in KNN-based ceramics. In this way, the density obtained by Archimedes' method was 4.47 g cm^{-3} and an average grain size of ~1.9 ± 0.8 μm. The high density KNL-(NTS)Mo ceramic is perfectly adapted to measure the dielectric, ferroelectric and piezoelectric properties, and to try to correlate such properties to

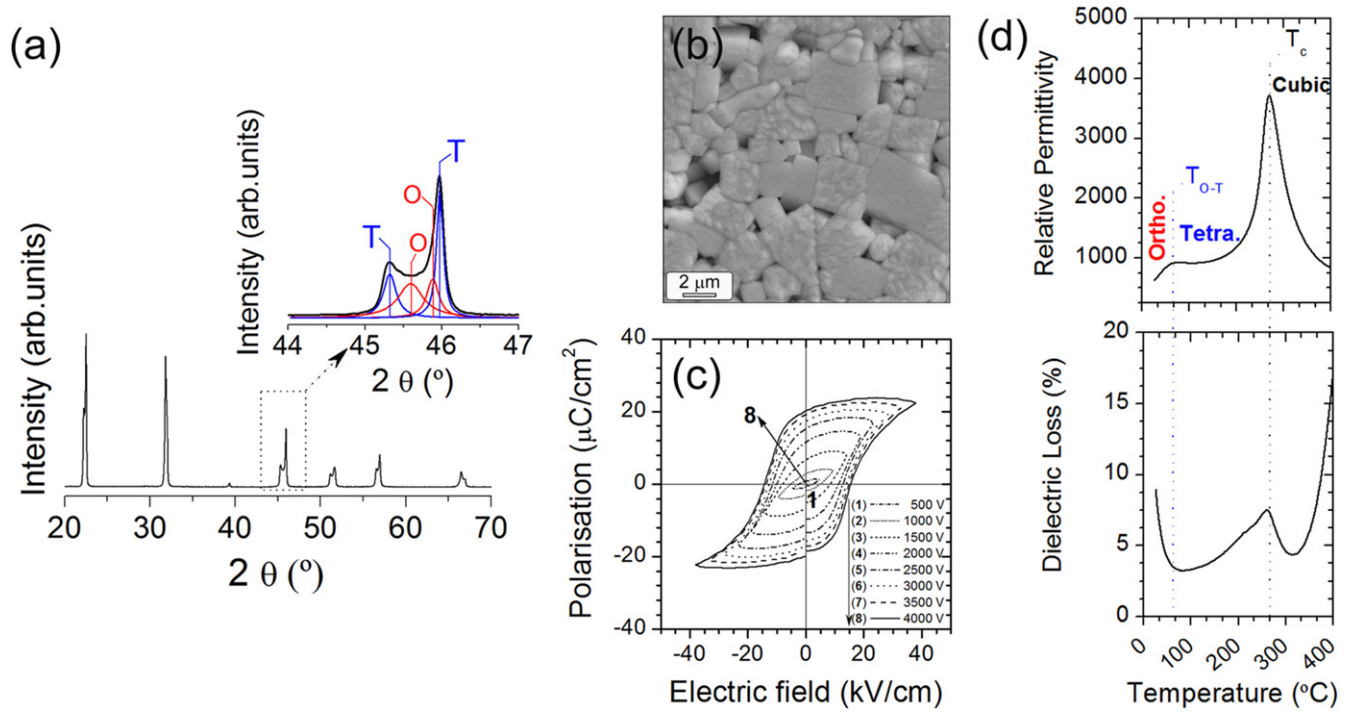

Figure 2. Structural, microstructural and electric characterization of KNL-(NTS)Mo ceramics: (a) XRD pattern corresponding to ceramic sintered at 1125 °C for 2 h. The inserts of the figure show a detail of the XRD diffraction pattern in the range 44.5–47°. (b) Microstructure of polished and thermally etched surfaces. (c) Hysteresis loops at room temperature. (d) Temperature dependence of the relative permittivity and of the dielectric losses (at 100 kHz).

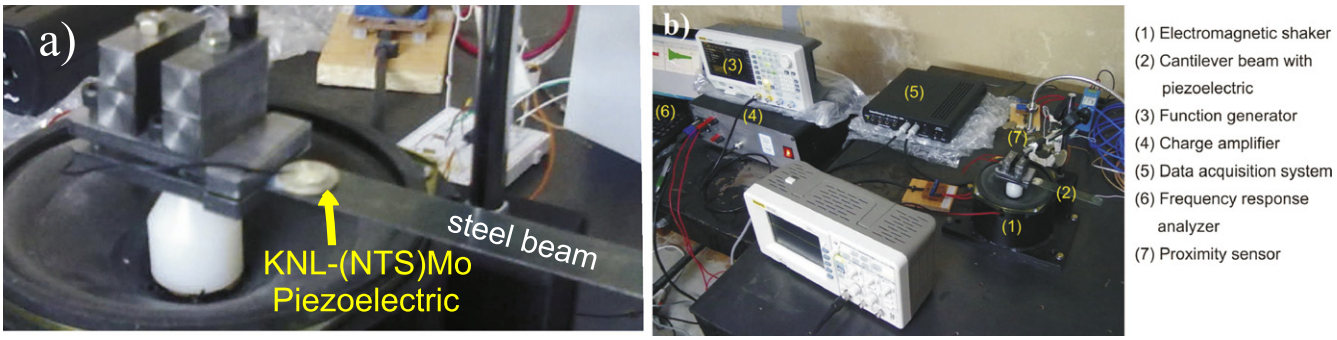

Figure 3. (a) Electromechanical system under study comprising a steel beam and a piezoelectric disc. (b) Experimental setup for the proposed system.

the observed structural evolution. Figure 2(c) shows the P-E loops of the ceramics as a function of applied electric field between 500 and 4000 V, measured at room temperature. One can see that the KNL-(NTS)Mo sample possesses typical polarization electric field (P-E) loops. The ceramic sample shows a remnant polarization (P_r) and saturation values (P_s) of ~20 μC cm^{-2} and 25 μC cm^{-2}, which are a little lower than PZT ceramics. In order to further determine the phase transition temperature, the temperature dependence of the relative permittivity, ϵ_r, and dielectric losses curves (at 100 kHz) of the KNL-(NTS)Mo sample were measured in the temperature range of 25–400 °C, as shown in figure 2(d). Considering the evolution of the dielectric constant, two anomalies are observed: (i) a sharp peak in Curie temperature, T_c, of 270 °C corresponding to the cubic (paraelectric)-tetragonal (ferroelectric) phase transition; and (ii) a weak maximum close to room temperature, corresponding to the tetragonal (ferroelectric)-orthorhombic (ferroelectric) phase transition, T_{O-T}. Considering the results of both XRD patterns and ϵ_r-T curves, see figures 2(a) and (d), we can deduce that the KNL-(NTS)Mo sample belongs to orthorhombic (O) and tetragonal (T) phase coexistence.

Finally, a sample was obtained in the form of a disc (16.12 mm diameter, 1.96 mm thick) which was bonded to a steel beam comprising the electromechanical system to be analyzed (see figure 3(a)).

4. Results and discussions

Analysis of the electromechanical system was performed for the first two modes. The actual setup for the experiment is

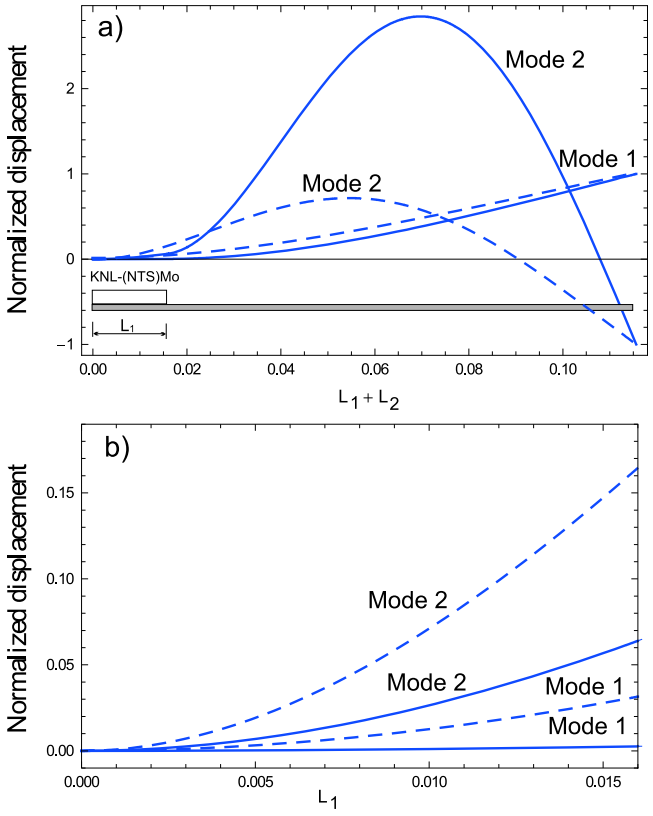

Figure 4. (a) First two normalized mode shapes for the electromechanical system as a function of its span (solid lines). (b) Enlargement of the zone where the KNL-(NTS)Mo is attached on the steel beam. Additionally, the first two normalized mode shapes of a cantilever beam (without the piezo disc) are shown for comparison (dashed lines).

Table 1. Geometrical and physical parameters of the electromechanical system consisting of a steel beam and a piezoelectric disc.

Geometrical parameters	Beam steel	Piezoelectric disc KNL-(NTS)Mo
Length, L (mm)	115.6	16.12 (diameter)
width, b (mm)	19	—
thickness, b (mm)	0.9	1.96
Material parameters		
density, ρ (kg m^{-3})	7800	4470
Young modulus, E (GPa)	210	105
piezo constant, d_{31}(m V^{-1})	—	-45×10^{-12}
Capacity, C_p (nF)	—	4.02
Dielectric constant	—	2650

illustrated in figure 3 and it includes an electrodynamic shaker for base excitation whose acceleration is measured by integrating twice the measurements of a displacement proximity sensor (Provibtech, TM0182, Houston, USA). Sinusoidal excitation is provided by a signal generator (Rigol, RTI-DG4062, Beijing, China) in a frequency sweep over the frequencies of interest and its power adjusted by a power amplifier (homemade; power 100W, bandwidth 1 Hz–50 Khz). All measured signals are then recovered for post-processing using a data acquisition system (Pasco Scientific, CI-7500, Roseville, USA), see figure 3(b).

In table 1 we present the physical and geometrical parameters of the steel beam and of the piezoceramic disc of KNL-(NTS)Mo.

Several experiments that show the voltage/power to base acceleration frequency response functions (FRFs) for frequencies near the first two modes of the system were performed to validate the electromechanical model of section 2. For the first mode, the reader may refer to figures 5(a) and (b) and for the second mode the results are shown in figures 6(a) and (b).

To analyze the experiments, it is useful to bear in mind the following theoretical concepts. The differences in generated voltage between the first and second mode can be explained by analyzing equation (1), which shows that the generated voltage is directly proportional to the piezoelectric coupling θ and mode coupling Γ. From the analytical results Γ was calculated, obtaining an equal value for both modes. Thus, the difference in generated voltage is caused by the piezoelectric coupling θ. By its definition, it depends on $e_{zx} = d_{31}c_{11}^{E}$ and on the attachment location of the piezoelectric disc through the first derivative of the mode shape evaluated at the span of the piezoelectric disc $\phi_j'(L_1)$(see equation (1) and below). Therefore, since $\phi_j'(L_1)$ depends on the mode shapes, any differences in the generated voltage can be attributed to this. In figures 4(a) and (b) we show the proposed normalized mode shapes of equation (2) as a function of the span of the electromechanical system. There, the different slopes are clearly observed in both modes. From this fact, it is evident that the selection of the mode shapes is very important to predict an accurate piezoeletric coupling.

Also in figures 4(a) and (b) we show for comparison in dashed lines the first two mode shapes of a cantilever beam (without the piezo disc). Thus it can be seen that the great differences in the slopes may lead to erroneous results if we do not choose the correct mode shapes.

The experiments shown in figures 5(a) and (b) present the voltage/power to base acceleration FRFs near the first mode of the system. Each experiment was performed by changing a set of five resistances whose values were: 986 kΩ, 247.8 kΩ, 89.6 kΩ, 31.7 kΩ and 9.85 kΩ. These values result from the equivalent resistance of commercial resistive loads connected in parallel with the input resistance of the data acquisition system. Note that all the values of voltage/power are divided by base acceleration to obtain a voltage/power to base acceleration FRF (in units of g = 9.81 m s^{-1}). In the case of voltage generation, the maximum value of V g^{-1} is ~4.8 V g^{-1} and corresponds to the maximum load resistance. The minimum value is approximately 0.08 V g^{-1} and corresponds

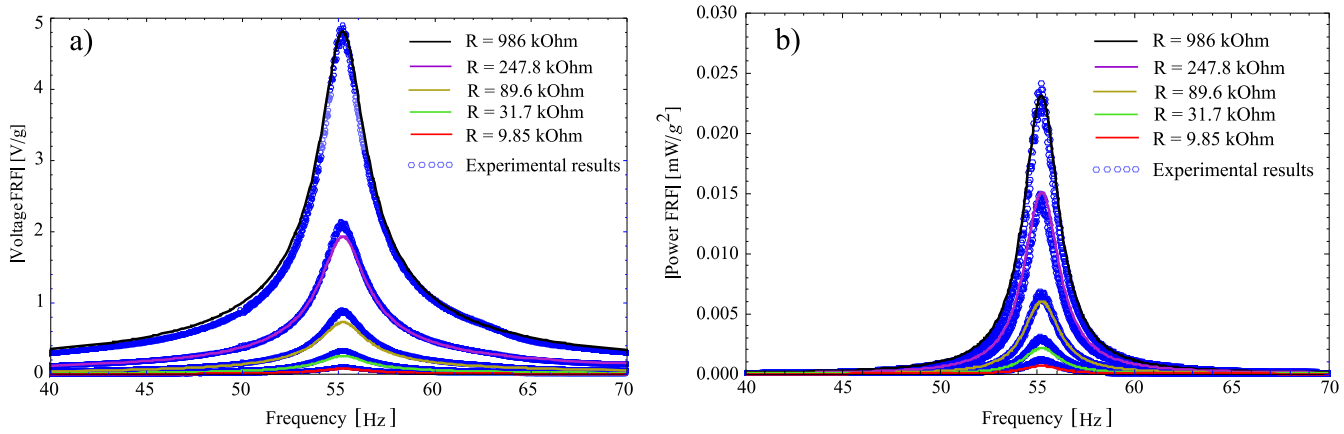

Figure 5. (a) Voltage to base acceleration FRFs for frequencies near the first mode of the electromechanical system for a given set of resistors. Blue circles represent experimental results, coloured lines represent theoretical results. (b) Power to base acceleration FRFs for frequencies near the first mode of the electromechanical system.

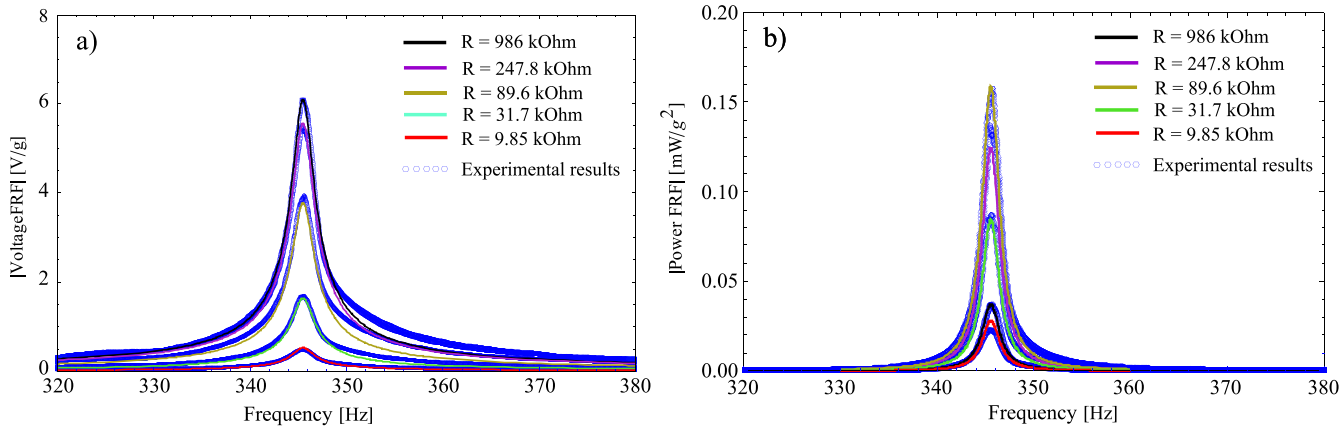

Figure 6. (a) Voltage to base acceleration FRFs for frequencies near the second mode of the electromechanical system for a given set of resistors. Blue circles represent experimental results, coloured lines represent theoretical results. (b) Power to base acceleration FRFs for frequencies near the second mode of the electromechanical system.

to the lowest resistance, which is the case of maximum current consumption.

From the voltage values obtained in figure 5(a) we calculate the electrical power generated for each resistive load as $P = V^2/R_l$ whose values can be observed in figure 5(b). The different curves show the electrical power for the resistances considered. The maximum generated power is 0.025 mW for resistance $R_l = 986\,\mathrm{k}\Omega$.

Figures 6(a) and (b) show the results for the generated voltage and power for frequencies near the second mode of the system. We can observe in this case that the generated voltage in figure 6(a) is greater than for the first mode. The maximum voltage is approximately ~6.1 V g^{-1}, which is almost 30% higher than the voltage for the first mode. The minimum voltage, however, is $0.52 \gtrsim$ V g^{-1}, which is more than six times the voltage generated for the first mode. Regarding the generated power which can be observed in figure 6(b), it is possible to observe a maximum generated power of 0.15 mW for a resistance of $R = 89.6\,\mathrm{k}\Omega$. Note that this value of resistance for the maximum generated power is different from the value obtained for the first mode.

4.1. Optimum electrical load

It is clear from our results (figures 5 and 6) that the value of the electrical load resistance that maximizes power depends on frequency. Then, it is possible to think about finding an optimum value that maximizes electrical power.

The electrical model considered here was extracted from [22] and used in equation (1) to obtain the voltage generation. It is worth pointing out that this is a simplified version of a more complete electrical model, encountered, for example, in [27, 28] where a series resistance ($R_s = \tan\delta/\Omega C_p$, δ dielectric loss factor) due to the capacitor is considered in the electrical model of the piezo. Physically, it is expected that the optimum load will be the one that matches the impedance of the capacitor [28]. In this sense, and in the absence of damping, this will be

$$R_l^{\mathrm{opt}} = \left\| \frac{1}{j\Omega C_p} \right\|, \tag{9}$$

($\|\ ..\ \|$ = modulus) which coincides with equation (6) in [28] for the case of $\delta = 0$(our model).

On the other hand, considering damping in the model will lead us to equation (1) for the voltage expression. Then, it is possible from this and the power definition $P = V^2/R_l$ to mathematically obtain an R_l value that maximizes power. It is straightforward to show that this is

$$R_l^{opt} = \frac{\omega_j^4 + \left(4\xi_j^2 - 2\right)\omega_j^2\Omega^2 + \Omega^4}{\sqrt{\Omega^2\left(\theta_j^4 + 2C_p\theta_j^2\left(\omega_j^2 - \Omega^2\right)\right) + C_p^2\left(\omega_j^4 + \left(4\xi_j^2 - 2\right)\xi_j^2\Omega^2 + \Omega^4\right)}}. \quad (10)$$

For the values considered in the experiments, this expression can be reduced to

$$R_l^{opt} = \frac{1}{C_p\Omega}, \quad (11)$$

in accordance with our physically deduced equation (9).

Finally, the calculated optimum resistance for the first mode is $R_l^{opt\,(1)} = 7.205 \times 10^5\Omega$ and $R_l^{opt\,(2)} = 1.1515 \times 10^5\Omega$ for the second mode. Evidently, these values are not in agreement with those obtained experimentally because they were selected for a commercial set of resistances.

4.2. Magnitude of the generated voltage

Regarding the magnitude of the generation of voltage, the values obtained experimentally were acceptable. Compared with other commercial piezoelectric materials such as PZT, generation was lower. For example, for a commercial PZT bimorph (T226-H4-203X) manufactured by Piezo Systems Inc, our KNL-(NTS)Mo possess a power density (power output divided by the volume of the piezo-device) of 0.0625 mW g^{-2} cm^{-3} against 2.1 mW g^{-2} cm^{-3} of the PZT, for frequencies near the first resonant mode of the piezo system. The specific power, which is power output divided by the total mass of the piezo device is 0.014 mW g^{-2}gr for the KNL-(NTS)Mo and 0.27 mW g^{-2}gr for the PZT device in the same interval of frequencies. However, there exist several parameters of this new material that can be optimized to obtain a larger voltage; for example, by optimizing the effective piezoelectric strain constant ϵ_{zx}, the physical dimensions of the disc or by attaching it to other locations on the hosting structure.

5. Conclusions

In summary, we carried out a series of dynamic experiments with a novel type of lead-free piezoelectric material KNL-(NTS)Mo attached to a vibrating steel beam. The main conclusion is that this new type of material KNL-(NTS)Mo can be used for energy harvesting when attached to a vibrating element such as a beam or other flexible structure. Regarding the modelling of the electromechanical system, there exists excellent agreement between the analytical (numerical) and experimental results, highlighting the validity of the analytical model. In the particular case of the system considered and ceramics characteristics such as density and composition of the main phase, maximum power generation occurs for the second mode, with a 10 times larger power compared to the first mode. This behaviour is due to the electromechanical coupling, which depends on the attachment position of the piezoelectric disc over the beam.

Acknowledgments

M Febbo acknowledges CONICET, Secretaría de Ciencia y Tecnología UNS and SPU under grant 'Enrique Mosconi'. S Machado acknowledges CONICET, SPU and Secretaría de Ciencia y Tecnología UTN-FRBB. M S Castro and L A Ramajo thank CONICET, ANPCyT and UNMdP for financial support. F Rubio-Marcos expresses his thanks to the MINECO (Spain) project MAT2013-48009-C4–1-P for their financial support. F Rubio-Marcos is also indebted to MINECO for a 'Juan de la Cierva' contract (ref: JCI-2012-14521), which is co-financed with FEDER funds.

References

[1] Wang Y, Tang B and Zhang S 2014 *Appl. Energy* **113** 59–66
[2] Sun D M, Wang K, Zhang X J, Guo Y N, Xu Y and Qiu L M 2013 *Appl. Energy* **106** 377–82
[3] Chiba S, Waki M, Wada T, Hirakawa Y, Masuda K and Ikoma T 2013 *Appl. Energy* **104** 497–502
[4] Delnavaz A and Voix J 2014 *Smart Mater. Struct.* **23** 105020
[5] Shu Y C and Lien I C 2006 *J. Micromech. Microeng.* **16** 2429–38
[6] Lee S and Jung B C 2009 *Smart Mater. Struct.* **18** 095021
[7] Jeon Y, Sood R, Jeong J H and Kim S G 2005 *Sensors Actuators* **122** 16–22
[8] Poulin G, Sarraute E and Costa F 2004 *Sensors Actuators* **116** 461–71
[9] Roundy S, Wright P K and Rabaey J 2003 *Comput. Commun.* **26** 1131–44
[10] Erturk A, Hoffmann J and Inman D J 2013 *Appl. Phys. Lett.* **94** 254102
[11] Erturk A, Vieira W GR, de Marqui C and Inman D J 2010 *Appl. Phys. Lett.* **96** 184103
[12] Vocca H, Neri I, Travasso F and Gammaitoni L 2012 *Appl. Energy.* **97** 771–6
[13] van den Ende D A, van de Wiel H, Groen W and van der Z 2012 *Smart Mater. Struct.* **21** 015011
[14] Pang X, Qiu J, Zhu K and Luo J 2011 *J. Mater. Sci.* **46** 2345–9
[15] Thongtha A and Bongkarn T 2011 *Eng. Mater.* **474** 1754–9
[16] Wang H, Zuo R, Liu Y and Fu J 2010 *J. Mater. Sci.* **45** 3677–82
[17] Saito Y, Takao H, Tani T, Nonoyama T, Takatori K, Homma T, Nagaya T and Nakamura M 2004 *Nature* **432** 84–87
[18] Rubio-Marcos F, Romero J J, Martín-Gonzalez M and Fernández J F 2010 *J. Eur. Ceram. Soc.* **30** 2763–71
[19] Roundy S and Wright P K A 2004 *Smart Mater. Struct.* **13** 11311144
[20] duToit N E, Wardle B L and Kim S 2005 *Integr. Ferroelectr.* **71** 121160
[21] Erturk A and Inman D J 2008 *J. Vib. Acous.* **130** 041002
[22] Erturk A and Inman D J 2009 *Smart. Mater. Struct.* **18** 025009

[23] Stanton S C, McGehee C C and Mann B P 2010 *Physica* D **239** 640–53
[24] Ramajo L, Castro M, Rubio-Marcos F and Fernandez-Lozano J 2013 *J. Mater. Sci., Mater. Electron.* **24** 3587–93
[25] Kakimoto K, Akao K, Guo Y and Ohsato H 2005 *Jpn. J. Appl. Phys.* **44** 7064–70
[26] Bortolani F, del Campo A, Fernandez J, Clemens F and Rubio-Marcos F 2014 *Chem. Mater.* **26** 3838–48
[27] Xu T B, Siochi E J, Kang J J, Zuo L, Zhou W, Tang X and Jiang X 2013 *Smart Mater. Struct.* **22** 065015
[28] Kim H, Priya S and Uchino A 2006 *Jpn. J. Appl. Phys.* **45** 5386–840